The Astrophysical Journal Letters, 808:L46 (7pp), 2015 August 1 doi:10.1088/2041-8205/808/2/L46

FIRST MEASUREMENTS OF ^{15}N FRACTIONATION IN N_2H^+ TOWARD HIGH-MASS STAR-FORMING CORES*

F. Fontani[1], P. Caselli[2], A. Palau[3], L. Bizzocchi[2], and C. Ceccarelli[4,5]
[1] INAF-Osservatorio Astrofisico di Arcetri, L.go E. Fermi 5, I-50125 Firenze, Italy
[2] Max Planck Institute for Extraterrestrial Physics, Giessenbachstrasse 1, D-85748 Garching, Germany
[3] Centro de Radioastronomía y Astrofísica, Universidad Nacional Autónoma de México, P.O. Box 3-72, 58090 Morelia, Michoacán, México
[4] Univ. Grenoble Alpes, IPAG, F-38000 Grenoble, France
[5] CNRS, IPAG, F-38000 Grenoble, France
Received 2015 March 5; accepted 2015 June 12; published 2015 July 30

ABSTRACT

We report on the first measurements of the isotopic ratio $^{14}N/^{15}N$ in N_2H^+ toward a statistically significant sample of high-mass star-forming cores. The sources belong to the three main evolutionary categories of the high-mass star formation process: high-mass starless cores, high-mass protostellar objects, and ultracompact H II regions. Simultaneous measurements of the $^{14}N/^{15}N$ ratio in CN have been made. The $^{14}N/^{15}N$ ratios derived from N_2H^+ show a large spread (from ∼180 up to ∼1300), while those derived from CN are in between the value measured in the terrestrial atmosphere (∼270) and that of the proto-solar nebula (∼440) for the large majority of the sources within the errors. However, this different spread might be due to the fact that the sources detected in the N_2H^+ isotopologues are more than those detected in the CN ones. The $^{14}N/^{15}N$ ratio does not change significantly with the source evolutionary stage, which indicates that time seems to be irrelevant for the fractionation of nitrogen. We also find a possible anticorrelation between the $^{14}N/^{15}N$ (as derived from N_2H^+) and the H/D isotopic ratios. This suggests that ^{15}N enrichment could not be linked to the parameters that cause D enrichment, in agreement with the prediction by recent chemical models. These models, however, are not able to reproduce the observed large spread in $^{14}N/^{15}N$, pointing out that some important routes of nitrogen fractionation could be still missing in the models.

Key words: ISM: molecules – molecular data – radio lines: ISM – stars: formation – submillimeter: ISM

1. INTRODUCTION

Nitrogen is the fifth most abundant chemical element in the universe and exists in the form of two stable isotopes: ^{14}N and ^{15}N. In the terrestrial atmosphere (TA), the typical atomic composition $^{14}N/^{15}N$ as derived from N_2 is ∼270. This value is quite consistent (within a factor of two) with that measured in cometary nitrile-bearing molecules (e.g., Bockelée-Morvan et al. 2008; Manfroid et al. 2009) and in primitive chondrites (e.g., Briani et al. 2009; Bonal et al. 2010), but it is significantly smaller than the value measured in the present-day solar wind, which is $\sim 441 \pm 6$, as derived from the particles collected by the *Genesis* spacecraft (Marty et al. 2011). This value is comparable to that of the Jupiter's atmosphere (Fouchet et al. 2004), and it is considered to be representative of the so-called "proto-solar nebula" (PSN), from which our Sun has formed. However, to understand how these values are linked to the initial chemical composition of the molecular environment in which the system itself was formed and put constraints on chemical models, measurements of the $^{14}N/^{15}N$ ratio in dense molecular star-forming cores similar to that in which the Sun was likely formed are mandatory.

In dense molecular cores, where the direct observation of N_2 is impossible, the $^{14}N/^{15}N$ isotopic ratio is measured from abundant N-bearing species such as N_2H^+, NH_3, CN, HCN, and HNC, and the results are still puzzling. In fact, while the $^{14}N/^{15}N$ ratio measured toward pre-stellar cores or protostellar envelopes in hydrogenated nitrogen compounds (such as N_2H^+ and NH_3) is comparable to the value found in the PSN (e.g., in NH_3; Gerin et al. 2009; Lis et al. 2010; Daniel et al. 2013), or even larger (1000 ± 200 in N_2H^+; Bizzocchi et al. 2013), the $^{14}N/^{15}N$ ratio derived from the nitrile-bearing species HCN and HNC is significantly lower (140–360, Hily-Blant et al. 2013a; 120–400, Adande & Ziurys 2012; 160–290, Wampfler et al. 2014). Differences in nitrogen hydrides and nitrile-bearing molecules within clouds are predicted by chemical models inclusive of spin-state chemistry (Wirström et al. 2012; Hily-Blant et al. 2013a), but no models so far have been able to reproduce the low ^{15}N fractions measured in N_2H^+. The ^{15}N fraction measured in CN toward starless cores has been found marginally consistent with the proto-solar value of 441 (500 ± 75; Hily-Blant et al. 2013b), in contrast with the large ^{15}N fractions measured in HCN in both starless cores (Hily-Blant et al. 2013b) and protostellar objects (Wampfler et al. 2014). This is also expected from theory (Hily-Blant et al. 2013b). A gradient of $^{14}N/^{15}N$ with the Galactic distance has been measured by Adande & Ziurys (2012) via observations of molecular clouds in CN and HCN and is found to be in agreement with predictions of Galactic chemical evolution models (e.g., Clayton 2003; Romano & Matteucci 2003). However, the ^{15}N fractionation of CN and HCN are often based on observations of the optically thin isotopologues containing ^{13}C because the main isotopologues are typically optically thick, which makes it less accurate the derivation of the column densities (e.g., Hily-Blant et al. 2013a, 2013b). Roueff et al. (2015) have found possible reduced abundances of the ^{13}C due to the fact that nitriles and isonitriles are predicted to be significantly depleted in ^{13}C (Roueff et al. 2015). However, this depletion is estimated to be of the order of ∼20%, namely,

* Based on observations carried out with the IRAM-30 m Telescope. IRAM is supported by INSU/CNRS (France), MPG (Germany), and IGN (Spain).

often of the order of the calibration uncertainties associated with the measured column densities.

In star-forming regions, D and ^{15}N fractions are not correlated. For example, in L1544, N_2H^+ is highly deuterated (D fraction ∼30%; Caselli et al. 2002), while an anti-fractionation is observed in ^{15}N (Bizzocchi et al. 2013). Wirström et al. (2012) reproduced these differentiations and noticed that they are also present in meteoritic material; as in only a few cases,^{14}N/^{15}N correlates with H/D ratios (Mandt et al. 2014). This suggests an interstellar heritage of the solar system ^{15}N and D isotopic anomalies. Therefore, it is important to gather more data and to put stringent constraints on current chemical models, with the ultimate goal of investigating the possible link between cometary and interstellar medium material (see also Caselli & Ceccarelli 2012), especially in intermediate- and high-mass dense cores, since growing evidence is suggesting that our Sun was born in a rich stellar cluster (Adams 2010).

In this Letter, we report the first observational measurements of the ^{14}N/^{15}N ratio in a sample of dense cores associated with different stages of the high-mass star formation process and already studied in deuterated molecules. Our study can investigate if the nitrogen fractionation process varies with the physical evolution of the core. What is more, the ^{14}N/^{15}N ratio is derived from two well-studied nitrogen-bearing species, N_2H^+ and CN, allowing us to investigate whether the fractionation of the two species follows different pathways as suggested by Hily-Blant et al. (2013a).

2. OBSERVATIONS

The spectra presented in this work are part of a spectral survey performed with the IRAM-30 m Telescope in two millimeter bands, one centered at about 3 mm covering frequencies in the range 89.11–96.89 GHz and another centered at about 1.3 mm covering frequencies in the range 216.0–223.78 GHz, toward 26 dense cores divided into 3 main evolutionary categories: high-mass starless cores (HMSCs), high-mass protostellar objects (HMPOs), and ultracompact H II regions (UC H IIs; see also Fontani et al. 2011 for details on the source selection criteria). In Fontani et al. (2015), we have published part of these observations, namely, that about the lines of CH_3OH and of its deuterated forms so that we refer to Section 2 and Table 2 of that work for a description of the observational parameters and technical details. In the 3 mm band, the fundamental rotational transition of N_2H^+, $^{15}NNH^+$, and $N^{15}NH^+$ (at 93173.4, 90263.8, and 91205.7 MHz, respectively) were observed simultaneously with the CH_3OH observations described by Fontani et al. (2015) with velocity resolution of ∼0.65 km s^{-1} (the telescope HPBW is ∼26″). In the 1 mm band, several hyperfine components of the transition $N = 2-1$ of radicals ^{13}CN (50 components with rest frequencies in between 217.0326 and 218.0311 GHz) and C^{15}N (10 components with rest frequencies in between 219.38749 and 219.93482 GHz) were also observed with a velocity resolution of ∼0.26 km s^{-1} (the telescope HPBW is ∼11″).

3. RESULTS

3.1. $^{15}NNH^+$, $N^{15}NH^+$, and N_2H^+

The $^{15}NNH^+$ (1–0) line has been detected in 14 cores: four HMSCs, six HMPOs, and four UC HIIs. Because the separation between the hyperfine components is comparable to the line widths, the hyperfine structure is unresolved in almost all spectra. Therefore, the lines have been fit with single Gaussians, except in four cases (05358–mm3, 05358–mm1, ON1, 19410) in which the fit to the hyperfine structure has given reliable results despite the small separation of the components and the poor spectral resolution. This simplified approach could affect the determination of the line width, but will not affect the measurement of the column densities because they will be derived from the total integrated area, as we will describe below. The $N^{15}NH^+$ (1–0) has been detected in 11 cores: two HMSCs, five HMPOs, and four UC HIIs. The hyperfine components in this case are only three, with a faint central one and two fainter satellites, but the faintness of the satellites has forced us to fit many of the lines with Gaussians in this case too. Finally, the N_2H^+(1–0) line is clearly detected in all sources, and the fit to the hyperfine structure gives good results in all spectra, pointing out that no hyperfine anomalies are present. In Figure 1, we show the spectra of the $^{15}NNH^+$, $N^{15}NH^+$, and N_2H^+ (1–0) lines in the representative core 05358–mm3.

The total column density of N_2H^+, averaged within the beam, has been evaluated from Equation (A1) in Caselli et al. (2002). The formula assumes the same T_{ex} for all the hyperfine components. For sources with the total opacity well constrained, T_{ex} was computed from the output parameters obtained from the hyperfine fit procedure (in particular, the total optical depth, τ_t, and $T_{ant} \times \tau_t$) following the approach described in the CLASS user manual.[6] For the others, we have assumed the average T_{ex} derived from the lines with well-constrained opacity in each evolutionary stage (18, 43, and 57 K for HMSCs, HMPOs, and UC H IIs, respectively) and obtained the column density from Equation (A4) of Caselli et al. (2002), valid for optically thin lines. The spectral parameters used in our calculations ($S\mu^2$, Einstein coefficients, rotational constants, energies, and statistical weight of the levels) were taken from the Cologne Database for Molecular Spectroscopy (Müller et al. 2005).

The total column densities of both $^{15}NNH^+$ and $N^{15}NH^+$ have been computed in all detected sources from the total line integrated intensity with Equation (A4) of Caselli et al. (2002), assuming optically thin lines and LTE conditions. As excitation temperature, we have used that derived from the N_2H^+(1–0) line. All column densities and the parameters used to derive them (line integrated intensities and T_{ex}) are given in Table 1.

3.2. ^{13}CN and $C^{15}N$

Several hyperfine components of the $N = 2-1$ transitions of both ^{13}CN and C^{15}N were detected toward 13 cores, which yield a detection rate of 50%. As expected, most of the cores were detected in the hyperfine components with larger values of $S\mu^2$, which are J, F_1, F = (5/2, 3, 4) − (3/2, 2, 3); (5/2, 3, 3) − (3/2, 2, 2); (5/2, 3, 2) − (3/2, 2, 1) for ^{13}CN, and J, F = (5/2, 3) − (3/2, 2); (5/2, 2) − (3/2, 1) for C^{15}N. Representative spectra obtained toward core 05358–mm3 centered on these hyperfine components are shown in Figure 1.

To compute the column densities of both radicals, we first have derived the integrated intensity of the group of hyperfine

[6] For details, see https://iram.fr/IRAMFR/GILDAS/doc/html/class-html/class.html/.

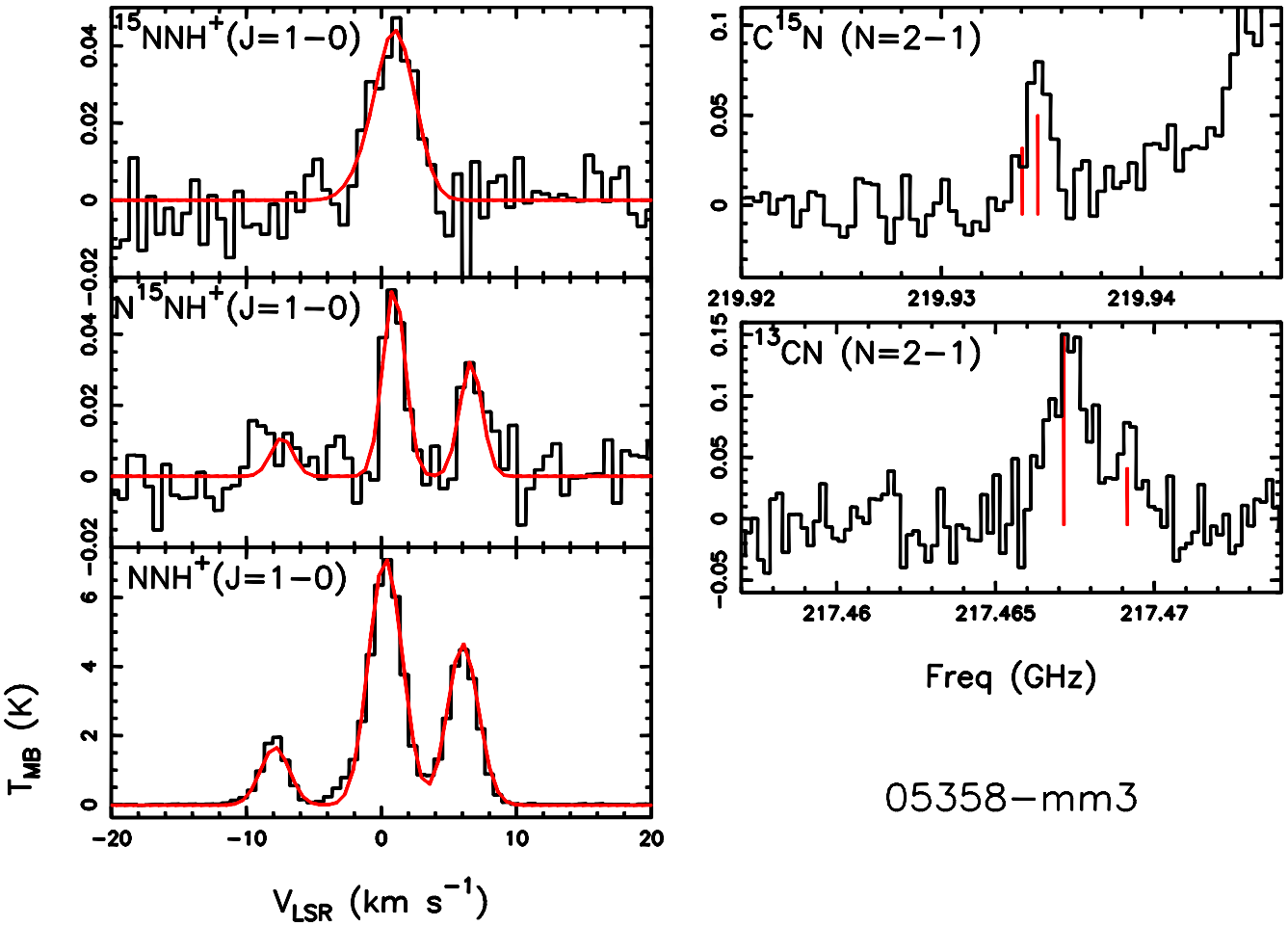

Figure 1. Left panels: spectra, from top to bottom, of $^{15}NNH^+$ (1–0), $N^{15}NH^+$ (1–0), and N_2H^+ (1–0) toward 05358–mm3. The velocity interval shown is ±20 km s^{-1} from the systemic velocity. For the $^{15}NNH^+$ line, the red curve represents the best Gaussian fit, while for the other lines, it corresponds to the best fit to the hyperfine structure. Right panels: spectra of $C^{15}N$ ($N = 2-1$; top) and ^{13}CN ($N = 2-1$; bottom) toward 05358–mm3 centered on the hyperfine components mentioned in Section 3.2 and indicated by the red vertical lines, the length of which is proportional to their relative intensities.

components (Table 2) mentioned above and then computed the total column densities from Equation (A4) of Caselli et al. (2002), which assumes the same excitation temperature in the various rotational levels, and it is valid for optically thin lines. The formula has been adapted to take the hyperfine structure into account, namely, we have adopted only the spectroscopic parameters (Einstein coefficients, energies, and statistical weight of the levels) of the hyperfine components considered. All spectroscopic parameters, as well as the partition functions used to derive the total column density, have been taken from the Cologne Database for Molecular Spectroscopy (Müller et al. 2005). When the hyperfine components are not blended, their relative intensities are consistent with the assumption of optically thin lines and no hyperfine anomalies (within the calibration uncertainties). As excitation temperature, we have used the T_{ex} reported in Table 1, derived from N_2H^+. This assumption is critical, but the $C^{15}N/^{13}CN$ column density ratio does not change by varying T_{ex} of even an order of magnitude, as it was already noted in other works dealing with isotopic ratios (see, e.g., Sakai et al. 2012; Fontani et al. 2014a).

The CN column densities were then computed from the ^{13}CN ones by applying the isotopic ratio $^{12}C/^{13}C$ derived from the relation between this ratio and the source galactocentric distance found for CN by Milam et al. (2005). Galactocentric distances have been taken from Fontani et al. (2014b). We have not corrected the column densities for a filling factor because we do not have any direct estimate of the size of the emitting region of both molecules, and we do not see any physical or chemical reason by which the emission of ^{13}CN and $C^{15}N$ should arise from different regions.

In 19410+2336 and ON1, the ^{13}CN hyperfine components mentioned above are barely detected, while in G5.89–0.39 they are heavily affected by a nearby CH_3OH stronger line. Therefore, in these sources, we have used the better detected hyperfine component J, F_1, $F = (3/2, 1, 1) - (1/2, 0, 1)$. In G5.89–0.39, the blending problem also affects the $C^{15}N$ lines so that we have used the isolated hyperfine component J, $F = (3/2, 2) - (1/2, 1)$ to compute the $C^{15}N$ column density. For I00117–MM1, I21307, I19035–VLA1, and 23033+5851, detected in ^{13}CN but not in $C^{15}N$, we have derived an upper limit for the column density of $C^{15}N$. All column densities, and the line integrated intensities used to compute them, are listed in Table 2.

4. DISCUSSION

The comparison between the column densities of the ^{15}N-containing species and those of their main isotopologues, derived as explained in Sections 3.1 and 3.2, is shown in

Table 1
Integrated Intensity of the $^{15}NNH^+$, $N^{15}NH^+$, and N_2H^+ (1–0) Transitions, Total Beam-averaged Column Densities Computed as Explained in Section 3.1, and Corresponding $^{14}N/^{15}N$ Isotopic Ratios

Source	$^{15}NNH^+$(1–0)		$N^{15}NH^+$ (1–0)		N_2H^+(1–0)		$\frac{N_2H^+}{^{15}NNH^+}$	$\frac{N_2H^+}{N^{15}NH^+}$	T_{ex}
	$\int T_{MB}dv$ (K km s^{-1})	$N(^{15}NNH^+)$ ($\times 10^{10}$ cm^{-2})	$\int T_{MB}dv$ (K km s^{-1})	$N(N^{15}NH^+)$ ($\times 10^{10}$ cm^{-2})	$\int T_{MB}dv$ (K km s^{-1})	$N(N_2H^+)$ ($\times 10^{13}$ cm^{-2})			(K)
HMSC									
I00117–MM2	0.029(0.001)[c]	5.68(0.09)	0.04	⩽6.8	3.966(0.007)[a]	3.8(0.5)	670(98)	⩾561	19
AFGL5142–EC[b]	0.040(0.002)	24(1)	0.04	⩽27	8.81(0.01)[a]	28(8)	1100(360)	⩾1034	76
05358–mm3[b]	0.17(0.01)	32(2)	0.20(0.01)	37(3)	39.69(0.05)	6.60(0.01)	210(12)	180(13)	18
G034–G2	0.04	⩽6.95	0.04	⩽6.8	4.314(0.001)[a]	5.95(0.08)	⩾856	⩾872	19
G034–F1	0.05	⩽6.94	0.04	⩽5.8	4.4(0.1)[a]	3.9(0.3)	⩾566	⩾672	11
G034–F2	0.04	⩽7.83	0.04	⩽6.6	9.20(0.03)	1.53(0.01)	⩾195	⩾232	18
G028–C1	0.04	⩽7.02	0.04	⩽5.9	5.735(0.006)[a]	8.5(0.1)	⩾1217	⩾1445	15
I20293–WC	0.063(0.006)	17(2)	0.08(0.01)	20(3)	7.150(0.003)[a]	11.0(0.8)	65(69)	550(98)	29
22134–G[b]	0.03	⩽5.6	0.04	⩽6.6	7.80(0.03)	1.30(0.01)	⩾232	⩾197	18
22134–B	0.04	⩽5.8	0.04	⩽5.7	2.83(0.07)[a]	1.8(0.3)	⩾316	⩾322	14
HMPO									
I00117–MM1	0.05(0.01)[c]	14(3)	0.05	⩽12.8	2.88(0.01)[a]	3.0(0.3)	220(60)	⩾233	27
AFGL5142–MM	0.072(0.009)	32(4)	0.042(0.003)[c]	18(1)	9.41(0.02)[a]	23.5(1)	740(97)	1300(210)	53
05358–mm1	0.17(0.02)	61(6)	0.18(0.02)	65(8)	36.63(0.05)	11.78(0.02)	190(20)	180(23)	43
18089–1732	0.08(0.09)	22(9)	0.10(0.01)	27(3)	9.312(0.002)[a]	21(2)	1000(400)	800(100)	31
18517+0437	0.058(0.008)	21(3)	0.089(0.005)	32(2)	25.98(0.03)	8.35(0.01)	390(53)	260(20)	43
G75–core	0.06	⩽22	0.05	⩽1.9	13.95(0.06)	4.49(0.02)	⩾209	⩾240	43
I20293–MM1	0.086(0.007)	56(5)	0.19(0.02)	122(14)	16.410(0.001)[a]	44.62(0.05)	790(67)	370(42)	82
I21307	0.05	⩽7.28	0.05	⩽6.3	2.13(0.05)[a]	2.2(0.3)	⩾301	⩾346	10
I23385	0.05	⩽19	0.06	⩽23	4.74(0.03)	1.53(0.01)	⩾81	⩾66	43
UC H II									
G5.89–0.39	0.18(0.01)	84(6)	0.13(0.01)	61(6)	66.3(0.5)	27.3(0.3)	320(25)	450(51)	57
I19035–VLA1	0.06	⩽31	0.05	⩽24	3.820(0.008)[a]	18(1)	⩾572	⩾754	66
19410+2336	0.18(0.02)	96(8)	0.16(0.01)	82(8)	21.27(0.01)[a]	43(5)	450(96)	500(100)	64
ON1	0.21(0.01)	72(3)	0.29(0.02)	94(8)	12.795(0.001)[a]	33(4)	460(22)	350(33)	39
I22134–VLA1	0.05	⩽24	0.04	⩽18	4.71(0.03)	1.94(0.01)	⩾80	⩾108	57
23033+5951	0.048(0.007)	23(3)	0.065(0.006)	30(3)	7.660(0.001)[a]	20(6)	900(400)	700(250)	57
NGC7538–IRS9	0.05	⩽24	0.05	⩽21	14.93(0.04)	6.13(0.02)	⩾255	⩾294	57

Notes. Uncertainties in the isotope ratios have been computed from the propagation of errors on the column densities. These have been derived from the errors on the line areas for the optically thin lines, given by rms $\times \Delta v \times \sqrt{N}$ (rms—root mean square noise in the spectrum, Δv—spectral velocity resolution, N—number of channels with signal). For the N_2H^+ (1–0) lines with well-constrained opacity, we propagated the errors on τ_i and $T_{ant} \times \tau_i$. The source names are taken from Fontani et al. (2011).

[a] Lines with well-constrained optical depth, for which we do not list the integrated intensity but the parameter $T_{ant} \times \tau_i$, from which we have derived the column density as explained in Section 3.1.

[b] "Warm" HMSC.

[c] Tentative detection.

Figure 2. The corresponding $^{14}N/^{15}N$ isotopic ratios are given in Tables 1 and 2. The first result emerging from these numbers and from Figure 2 is that the $NNH^+/^{15}NNH^+$ and $NNH^+/N^{15}NH^+$ ratios vary between 180 and 1300, namely, over a range much larger than observed so far toward low-mass objects in any N-bearing species. Some values, therefore, are compatible with both those of the TA and PSN, but much larger values are also measured. In addition, there is no evidence of a trend of these ratios with the evolution because Figure 2 shows that the sources belonging to different evolutionary stages possess similar $^{14}N/^{15}N$ ratios, within the uncertainties. Consistently, we do not find any correlation with the line widths, which are thought to be good indicators of the evolutionary stage. Therefore, whatever the reason for this different ^{15}N enrichment, time does not seem to play a role.

The second result is that the $CN/C^{15}N$ ratio is within ~190 and ~450, namely, consistent (within the errors) with the ^{15}N enrichment of both TA and PSN. Interestingly, when the $NNH^+/^{15}NNH^+$ and $CN/C^{15}N$ ratios can be measured in the same object, they have the same $^{14}N/^{15}N$ ratio, within the error bars, only in nearly half of the sources detected in both N_2H^+ and CN isotopologues, as shown in Figure 3. However, globally, the lower range of variation of the $CN/C^{15}N$ could be a result biased by the fact that fewer sources were detected in $C^{15}N$ than in the N_2H^+ isotopologues. Follow-up higher sensitivity observations will be helpful to address this aspect.

Note that since the $CN/C^{15}N$ has been derived by observations of ^{13}CN, there is also the possibility that an error is introduced because of the variation of the $^{12}C/^{13}C$ introduced by possible depletion of ^{13}C (see Section 1). However, the

Table 2
Integrated Intensity of the $C^{15}N$ and ^{13}CN Transitions, Total Beam-averaged Column Densities Computed as Explained in Section 3.2, and Corresponding $^{14}N/^{15}N$ Isotopic Ratio

Source	$C^{15}N(2–1)$		$^{13}CN(2–1)$			$\frac{N(CN)}{N(C^{15}N)}$
	$\int T_{MB} dv$ (K km s^{-1})	$N(C^{15}N)$ ($\times 10^{12}$ cm^{-2})	$\int T_{MB} dv$ (K km s^{-1})	D_{GC} (kpc)	$N(CN)$ ($\times 10^{14}$ cm^{-2})	
HMSC						
I00117–MM2						
AFGL5142–EC[a]	0.14(0.02)[c]	1.6(0.2)	0.35(0.02)[b]	10.3	5.3(0.3)	330(67)
05358–mm3[a]	0.12(0.02)[c]	0.7(0.1)	0.36(0.02)[b]	10.3	2.7(0.1)	400(90)
G034–G2	…	…	…	…	…	…
G034–F1	…	…	…	…	…	…
G034–F2	…	…	…	…	…	…
G028–C1	…	…	…	…	…	…
I20293–WC	…	…	…	…	…	…
22134–G[a]	0.06(0.02)[c]	0.3(0.1)	0.16(0.02)[b]	9.5	1.1(0.1)	330(150)
22134–B	…	…	…	…	…	…
HMPO						
I00117–MM1	⩽0.06	⩽0.4	0.13(0.02)[b]	9.5	1.0(0.1)	⩾250
AFGL5142–MM	0.28(0.02)[c]	2.4(0.2)	0.40(0.02)[b]	10.3	4.7(0.2)	190(23)
05358–mm1	0.12(0.02)[c]	1.5(0.2)	0.36(0.02)[b]	10.3	3.7(0.2)	240(40)
18089–1732	0.14(0.03)[c]	0.9(0.2)	0.80(0.02)[b]	5.1	4.0(0.1)	450(100)
18517+0437	0.10(0.02)[c]	0.8(0.2)	0.34(0.02)[b]	6.5	2.4(0.2)	310(80)
G75–core	0.19(0.03)[c]	1.4(0.2)	0.40(0.02)[b]	8.4	3.4(0.2)	240(50)
I20293–MM1	…	…	…	…	…	…
I21307	⩽0.06	⩽0.4	0.09(0.02)[b]	9.3	0.7(0.2)	⩾175
I23385	…	…	…	…	…	…
UC H II						
G5.89–0.39	0.14(0.03)[e]	3.5(0.8)	0.12(0.03)[d]	7.2	12(3)	350(160)
I19035–VLA1	⩽0.06	⩽0.6	0.16(0.02)[b]	7.0	1.6(0.2)	⩾270
19410+2336	0.07(0.02)[e]	1.9(0.5)	0.07(0.02)[d]	7.7	8(2)	430(250)
ON1	0.07(0.02)[e]	1.4(0.4)	0.06(0.02)[d]	8.0	5(2)	350(220)
I22134–VLA1	0.09(0.02)[c]	0.8(0.2)	0.18(0.02)[b]	9.5	2.1(0.2)	250(84)
23033+5951	⩽0.07	⩽0.7	0.21(0.02)[b]	10.3	2.6(0.2)	⩾370
NGC7538–IRS9	0.08(0.02)[c]	0.7(0.2)	0.14(0.02)[b]	9.9	1.7(0.2)	230(90)

Notes. We do not list the upper limits of the integrated intensity of ^{13}CN and $C^{15}N(2–1)$ for the sources undetected in both transitions. To compute $N(CN)$, the ^{13}CN column density was corrected by the $^{12}C/^{13}C$ ratio at the source galactocentric distance, D_{GC} (Col. 5), assuming the relation between $^{12}C/^{13}C$ and D_{GC} derived for CN by Milam et al. (2005). Uncertainties have been derived as explained in the caption of Table 1 for the optically thin lines.
[a] "Warm" HMSC.
[b] From the hyperfine components J, F_1, $F = (5/2, 3, 4) - (3/2, 2, 3)$, $(5/2, 3, 3) - (3/2, 2, 2)$, and $(5/2, 3, 2) - (3/2, 2, 1)$.
[c] From the hyperfine components J, $F = (5/2, 3) - (3/2, 2)$, and J, $F = (5/2, 2) - (3/2, 1)$.
[d] From the hyperfine component J, F_1, $F = (3/2, 1, 1) - (1/2, 0, 1)$.
[e] From the hyperfine component J, $F = (3/2, 2) - (1/2, 1)$.

recent, very detailed study by Roueff et al. (2015) predicts variations up to ∼20% ($CN/^{13}CN$ ratio from 67 to 80), namely, within the errors of our measurements. Thus, we conclude that our estimates of the $CN/C^{15}N$ are substantially correct.

The measurements of both $NNH^+/^{15}NNH^+$ and $CN/C^{15}N$ are at odds with the recent model by Roueff et al. (2015), which predicts that the $^{14}N/^{15}N$ should not vary in both species, unless the age of the condensation is shorter than 10^5 years. This possibility, however, seems to be ruled out by our observations, as the $^{14}N/^{15}N$ is not different in the three evolutionary groups. We conclude that some important routes of nitrogen fractionation are still missing in the models.

A hint of what they could be might be obtained considering the D fractionation of NNH^+ toward the same sources where we measured the N fractionation. The bottom panels in Figure 2 show $NNH^+/^{15}NNH^+$ and $NNH^+/N^{15}NH^+$ as a function of the NNH^+/NND^+, as previously measured by Fontani et al. (2011). Although not very strong, the data show a possible anticorrelation between the two parameters: the larger the $^{14}N/^{15}N$, the lower the H/D. Non-parametric statistical tests confirm this trend: the Kendall's τ rank correlation coefficient is ~ -0.5 when the $^{14}N/^{15}N$ is derived from either $^{15}NNH^+$ and $N^{15}NH^+$, and the Pearson's correlation coefficient is ~ -0.6 and -0.5, respectively. Moreover, the probability for a chance correlation is below 2% in both cases. Also, we have performed least square fits to the data, which provide slopes of −0.98 and −0.80 for the $^{14}N/^{15}N$ ratios derived from $^{15}NNH^+$ and $N^{15}NH^+$, respectively. Based on this suggestive anticorrelation, we conclude that the N fractionation does not seem to be linked to the parameters that are known to affect the D fractionation (if not to obtain the inverse effect): temperature and CO depletion (or density). In other words, the reactions leading to N

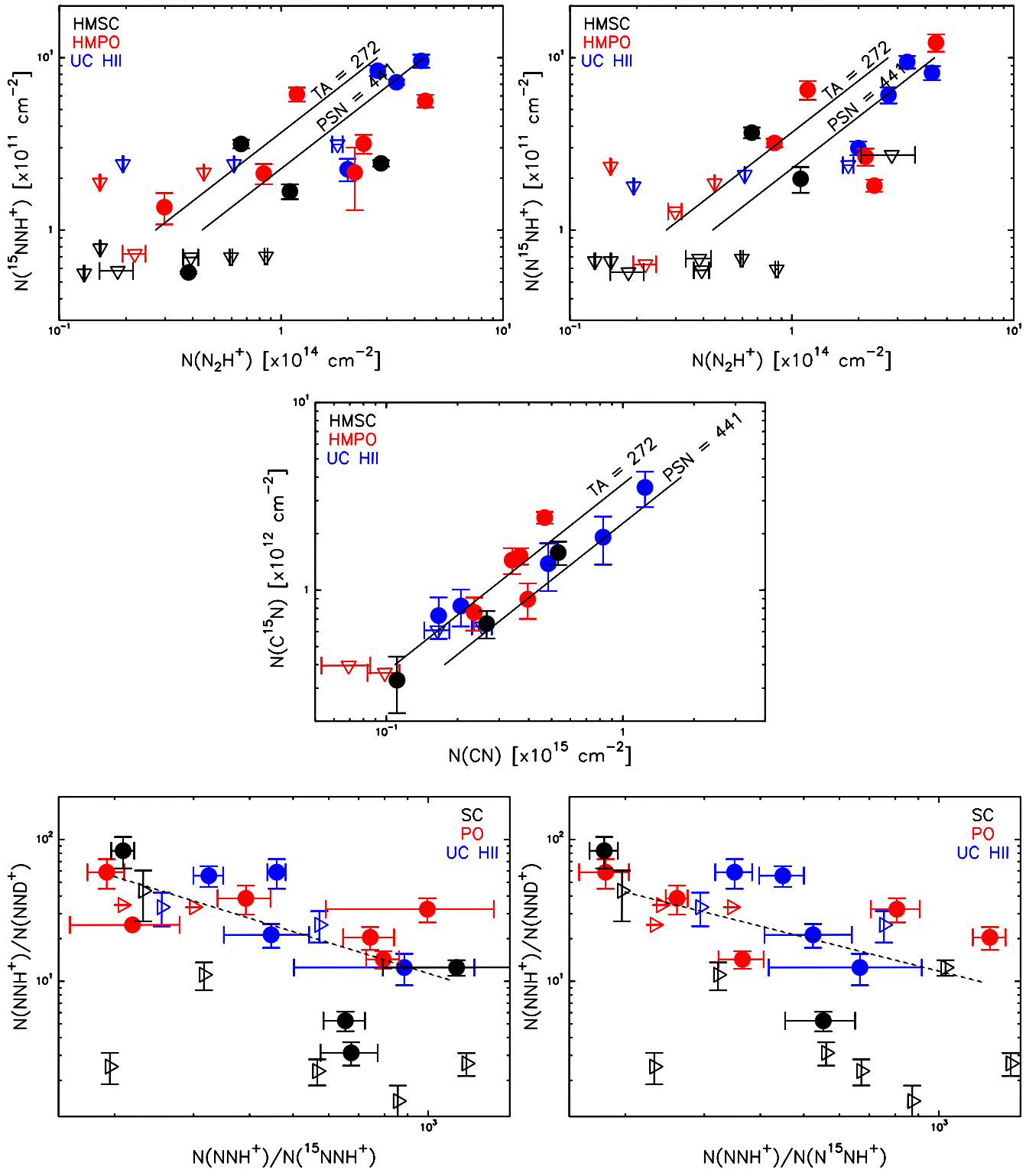

Figure 2. Top panels: column density of N_2H^+ against that of $^{15}NNH^+$ (left) and $N^{15}NH^+$ (right). Middle panel: column density of CN against that of $C^{15}N$. Bottom panels: comparison between the $^{14}N/^{15}N$ isotopic ratio as derived from the column density ratios $N(N_2H^+)/N(^{15}NNH^+)$ (left) or $N(N_2H^+)/N(N^{15}NH^+)$ (right), and the H/D isotopic ratio $N(N_2H^+)/N(N_2D^+)$. In all panels, the filled circles represent the detected sources (black = HMSCs; red = HMPOs; blue = UC HIIs). The open triangles in the top and middle panels correspond to the upper limits on $N(^{15}NNH^+)$, $N(N^{15}NH^+)$, or $N(C^{15}N)$, respectively, while in the bottom panels, they indicate lower limits on either $N(N_2H^+)/N(^{15}NNH^+)$ or $N(N_2H^+)/N(N^{15}NH^+)$. The solid lines indicate the mean atomic composition as measured in the terrestrial atmosphere (TA) and in the proto-solar nebula (PSN; see Hily-Blant et al. 2013a and references therein). The dashed lines in the bottom panels indicate least square fits.

fractionation of NNH^+ and CN indeed do not have an energy barrier, as predicted by Roueff et al. (2015). Finally, and consistently with this last sentence, we do not find any correlation between the measured N fractionation and the excitation temperature, contrary to the results of Wampfler et al. (2014), who claimed a tentative trend toward a

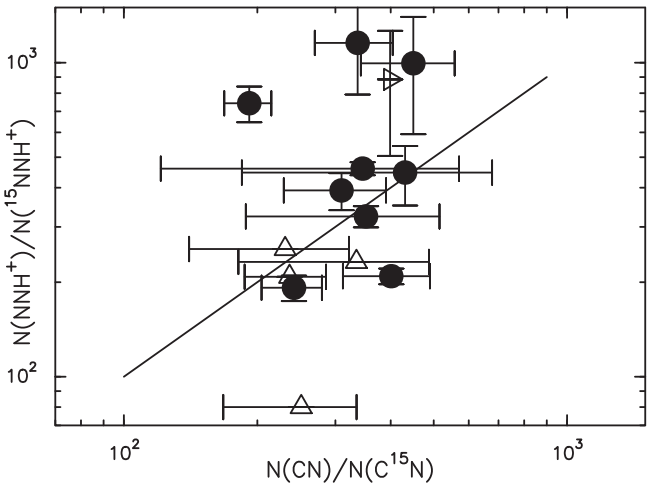

Figure 3. Comparison between the $^{14}N/^{15}N$ isotopic ratio as derived from N_2H^+ (y axis) and CN (x axis). On the y axis we report only the ratio $N(N_2H^+)/N(^{15}NNH^+)$, but the result is similar when using $N^{15}NH^+$. The filled circles represent the cores detected in both $^{15}NNH^+$ and $C^{15}N$. The open triangles with vertex pointing up correspond to lower limits on $^{14}N/^{15}N$ from N_2H^+, the one with vertex pointing right is the lower limit on $^{14}N/^{15}N$ from CN for 23033+5951. The straight line indicates the locus where $^{14}N/^{15}N$ from N_2H^+ and CN are the same.

temperature-dependent $^{14}N/^{15}N$ fractionation. However, because the anticorrelation found is not strong, care needs to be taken in the interpretation of this result.

5. CONCLUSIONS

We have observed the $J = 1$–0 rotational transitions of $^{15}NNH^+$, $N^{15}NH^+$, and N_2H^+, together with $N = 2$–1 transitions of ^{13}CN and $C^{15}N$, toward 26 massive star-forming cores in different evolutionary stages, where the deuteration fraction has already been measured (Fontani et al. 2011). We find $^{14}N/^{15}N$ in CN between ∼190 and ∼450 and in N_2H^+ from ∼180 up to ∼1300. It is the first time that high ^{15}N fractionations are found in N_2H^+. However, in the fractionation process, time does not seem to play a role because the $^{14}N/^{15}N$ ratio does not depend on the evolutionary stage of the source. We find a suggestive anticorrelation between D and ^{15}N fractions, consistent with findings in solar system material, where N isotope ratios largely vary and in only a few cases they have been found to correlate with D/H ratios (Mandt et al. 2014). This lack of correlation is also consistent with the prediction of chemical models, which rule out any link between fractionation of N and the causes of D enrichment, namely, temperature and density (or CO depletion).

F.F. and A.P. thank the IRAM staff for precious help during the observations. F.F. is grateful to Fabien Daniel for careful and constructive reading of the paper. P.C. acknowledges financial support of the European Research Council (ERC; project PALs 320620). A.P. acknowledges financial support from UNAM-DGAPA-PAPIIT IA102815 grant, México. This work has benefited from research funding from the European Community's Seventh Framework Programme.

REFERENCES

Adams, F. C. 2010, ARA&A, 48, 74
Adande, G. R., & Ziurys, L. M. 2012, ApJ, 744, 194
Bizzocchi, L., Caselli, P., Leonardo, E., & Dore, L. 2013, A&A, 555, AA109
Bockelée-Morvan, D., Biver, N., Jehin, E., et al. 2008, ApJ, 679, 49
Bonal, L., Huss, G. R., Krot, A. N., et al. 2010, GeCoA, 74, 6590
Briani, G., Gounelle, M., Marrocchi, Y., et al. 2009, LPSC, 40, 1642
Caselli, P., & Ceccarelli, C. 2012, A&ARv, 20, 56
Caselli, P., Walmsley, C. M., Zucconi, A., et al. 2002, ApJ, 565, 344
Clayton, D. 2003, in Handbook of Isotopes in the Cosmos, ed. D. Clayton (Cambridge: Cambridge Univ. Press), 326
Daniel, F., Gerin, M., Roueff, E., et al. 2013, A&A, 560, 3
Fontani, F., Busquet, G., Palau, A., et al. 2015, A&A, 575, 87
Fontani, F., Codella, Ceccarelli, C., et al. 2014a, ApJL, 788, L43
Fontani, F., Palau, A., Caselli, P., et al. 2011, A&A, 529, L7
Fontani, F., Sakai, T., Furuya, K., et al. 2014b, MNRAS, 440, 448
Fouchet, T., Irwin, P. G. J., Parrish, P., et al. 2004, Icar, 172, 50
Gerin, M., Marcelino, N., Biver, N., et al. 2009, A&A, 498, L9
Hily-Blant, P., Bonal, L., Faure, A., & Quirico, E. 2013a, Icar, 223, 582
Hily-Blant, P., Pineau des Forêts, G., Faure, A., le Gal, R., & Padovani, M. 2013b, A&A, 557, AA65
Lis, D. C., Wootten, A., Gerin, M., & Roueff, E. 2010, ApJL, 710, L49
Mandt, K. E., Mousis, O., Lunine, J. I., & Gautier, D. 2014, LPSC, 45, 1955
Marty, B., Chaussidon, M., Wiens, R. C., Jurewicz, A. J. G., & Burnett, D. S. 2011, Sci, 332, 1533
Manfroid, J., Jehin, E., Hutsemékers, D., et al. 2009, A&A, 503, 613
Milam, S. N., Savage, C., Brewster, M. A., Ziurys, L. M., & Wyckoff, S. 2005, ApJ, 634, 1126
Müller, H. S. P., Schlöder, F., Stutzki, J., & Winnewisser, G. 2005, JMoSt, 742, 215
Romano, D., & Matteucci, F. 2003, MNRAS, 342, 185
Roueff, E., Loison, J. C., & Hickson, K. M. 2015, A&A, 576, 99
Sakai, T., Sakai, N., Furuya, K., Aikawa, Y., et al. 2012, ApJ, 747, 140
Wampfler, S. F., Jørgensen, J. K., Bizzarro, M., & Bisschop, S. E. 2014, A&A, 572, 24
Wirström, E. S., Charnley, S. B., Cordiner, M. A., & Milam, S. N. 2012, ApJL, 757, L11